NASA Technical Memorandum 88831

Viscous Analyses for Flow Through Subsonic and Supersonic Intakes

Louis A. Povinelli and Charles E. Towne
Lewis Research Center
Cleveland, Ohio

Prepared for the
AGARD Propulsion and Energetics Panel Meeting on
Engine Response to Distorted Inflow Conditions
Munich, Germany, September 8-9, 1986

NASA

Viscous Analyses for Flow Through Subsonic and Supersonic Intakes

Louis A. Povinelli and Charles E. Towne
National Aeronautics and Space Administration
Lewis Research Center
Cleveland, Ohio 44135 U.S.A.

E-3209

SUMMARY

A parabolized Navier-Stokes code was used to analyze a number of diffusers typical of a modern inlet design. The effect of curvature of the diffuser centerline and transitioning cross sections was evaluated to determine the primary cause of the flow distortion in the duct. Results are presented for S-shaped intakes with circular and transitioning cross sections. Special emphasis is placed on verification of the analysis to accurately predict distorted flow fields resulting from pressure-driven secondary flows. The effect of vortex generators on reducing the distortion of intakes is presented. Comparisons of the experimental and analytical total pressure contours at the exit of the intake exhibit good agreement. In the case of supersonic inlets, computations of the inlet flow field reveal that large secondary flow regions may be generated just inside of the intake. These strong flows may lead to separated flow regions and cause pronounced distortions upstream of the compressor.

INTRODUCTION

The importance of computational fluid dynamics as an analysis tool for external flow about aircraft and aerospace configurations has been illustrated in the literature on numerous occasions. Less clearly demonstrated, however, has been the applicability of computational methods for internal flows in propulsion systems. Clearly, a need exists for analyzing the components of engine systems. In particular, the effect of intake design on air flow quality at the compressor face constitutes the initial step required in the overall flow analysis. High performance aircraft frequently employ complex intake ducting which, in turn, leads to highly three-dimensional flows. The complexity of the intake may include changes in curvature, cross-sectional area and out-of-plane bends. These geometric changes lead to cross-stream pressure gradients which drive secondary flows along the walls, and possibly result in strong vortex flow or separations. There exists a critical need, therefore, to properly model and calculate the flow in a variety of intake shapes in order to ensure reasonable flow quality to the engine over a wide flight range.

Numerous approaches have been used for the analysis of the flow for intake ducts. Inviscid computations coupled with a boundary layer analysis appear inadequate to describe the flow since the boundary layer thickness can grow to be a major portion of the duct height. Euler solvers can yield the velocity field but will not account for the viscous pressure losses. Fully elliptic Navier-Stokes solutions can provide an accurate flow field, but require hours of computer time. In addition, the grid size that can be efficiently analyzed is limited by computer storage for the full Navier-Stokes solutions. Computation time becomes important in the preliminary design process where a large number of intake configurations and operating conditions are analyzed. Parabolized Navier-Stokes solvers (PNS), however, offer a considerable reduction in computer time by making a single pass through the duct. Coupling of the elliptic pressure field with a fast PNS solver offers many desirable features. The PNS solvers are more economical than the full Navier-Stokes equations and less expensive to operate on present-generation computers. Most importantly, the PNS codes have been shown to yield accurate predictions within their domain of applicability.

This paper presents a review of the viscous analyses used by the NASA Lewis Research Center for application to aircraft intakes and the ducting upstream of the compressor. The computer methods discussed are based on the PNS equations. Analytical and experimental secondary flow and distortion patterns are reviewed for subsonic as well as high speed intakes.

APPROACH

The approach used in this paper is to review a number of computational studies for which selected aerodynamic parameters have also been measured, and to arrive at conclusions regarding our predictive capability for intakes. Three separate flow cases will be reviewed in sequence. A brief description of each study will be presented, including, as appropriate, the intake geometries, starting conditions, analysis method, grid size, experimental measurements and computational results of pressure and velocity. Each of the three cases will be examined as to the adequacy of the computational scheme to predict reasonable values. On the basis of the comparison, an evaluation or assessment of the predictive capability of the PNS solvers will be presented. In addition, potential difficulties associated with the PNS codes will be identified. Specific examples will also be discussed regarding the needs for additional code verification.

The three cases chosen for review involved an examination of:

(1) Pressures and velocities for intakes with centerline curvature and cross-sectional shape transitioning (Ref. 1).

(2) Secondary flows and total pressure coefficients for an S-duct with and without vortex generators (Ref. 2).

(3) Mach number and secondary velocities in a Mach 5 inlet, including spillage effects (Refs. 3 and 4).

The paper now proceeds to the Results section in which the three flow cases will be discussed in sequential fashion.

RESULTS

Centerline Curvature and Cross Section Transitioning (Ref. 1)

Summary of Analysis Method. Subsonic intakes at Lewis are typically studied using a three-dimensional PNS computer code (Refs. 5 to 7). This analysis is compressible and fully viscous. The flow is computed by a single sweep spatial marching procedure which solves an approximate form of the Navier-Strokes equations. It is assumed that the flow is primarily in the direction of the duct centerline, with transverse secondary flow. This allows two basic assumptions to be made. The first is that second derivatives in the primary flow direction are negligible. The second is that the pressure in the primary, or streamwise, momentum equation can be represented during a marching step by the sum of a known three-dimensional pressure field and a one-dimensional correction for viscous blockage. A two-dimensional pressure correction Poisson equation is also solved after each step to ensure that the computed velocity and pressure fields are consistent. The known three-dimensional pressure field can be obtained from any available source. Normally a potential flow solution is used. When these assumptions are applied to the Navier-Stokes equations, a set of equations can be derived that can be solved by forward marching in the primary flow direction. The equations are solved in a body-fitted nonorthogonal coordinate system using an implicit finite-difference technique. The analysis has been verified by comparing computed results with benchmark experimental data for a variety of duct configurations and flow conditions (Refs. 6 to 10).

Duct Configurations and Inlet Conditions. Examples of the types of geometries studied with this analysis are shown in Fig. 1. These configurations were used to investigate the effects of centerline curvature and cross section transitioning on the distortion in modern complex intake ducts (Ref. 1). The first, called the baseline configuration, represents a typical modern intake design. The cross section is represented by a superellipse, and transitions from nearly rectangular at the inlet to circular at the exit. The exit-to-entrance area ratio is 1.31. The other two configurations are derived from the first, and were used to isolate the effects of cross section transitioning and centerline curvature on the flow. The second configuration has the same distribution of cross section shape, but with a straight centerline. The third configuration has the same centerline shape and area distribution as the baseline configuration, but with a circular cross section.

Conditions used at the inlet were a total pressure of 800 psf and a Mach number of 0.5. This corresponds to flight at about 28 000 ft altitude. An initial turbulent boundary layer thickness equal to 4.8 percent of the duct half width was used for the baseline and straight centerline configurations. For the circular cross section configuration a thickness of 5.6 percent was used to give the same inlet blockage.

Computed Results. The effect of centerline curvature on flow distortion was determined by analyzing the circular cross section configuration of Fig. 1(c). In Fig. 2 the computed secondary flow field is shown at six stations through the duct. At the first station the cross flow velocities are small. The effect of the first bend can be seen at station b. The core flow moves toward the left side of the duct, responding to centrifugal effects. The low energy boundary layer flow moves away from the pressure side of the duct, on the left, toward the suction side of the duct, on the right. A vortex motion thus begins to develop but is quickly dissipated, as shown by the results at station c, when the cross flow pressure gradients reverse in the second bend. At station c the secondary flow in the boundary layer has reversed direction, flowing toward the low pressure region now on the left side of the duct. By station d a pair of counter rotating vortices has formed. These persist into the third bend and continue to move the low energy flow toward the left side of the duct. By station e the cross flow pressure gradients have again reversed direction, causing the formation of an additional pair of counter rotating vortices in the left half of the duct. Theses two pairs of vortices interact, driving the low energy flow away from the wall.

In Fig. 3 the distortion resulting from these secondary flows is shown in the form of constant total pressure contours at the six stations. The total pressure values are referenced to the inlet total pressure. The thickened boundary layer on the right side of the duct at station c is a result of the vortex pattern shown at station b in Fig. 2. As previously described, these vortices dissipate and a new pair is set up in the second bend. These persist into the third bend, where another pair develops. The two pairs of vortices interact, driving the low energy flow away from the wall, as shown by the bulges in the total pressure contours at stations e and f.

The computed secondary flow field for the baseline configuration of Fig. 1(a) is presented in Fig. 4. Even though this duct has the additional geometric complication of a transitioning cross section, the physics of the flow are essentially the same as in the circular cross section configuration just discussed. The same types of vortices are present, and they result in the same type of distortion pattern, as shown by the total pressure contours in Fig. 5. This indicates that for this intake duct the effect of the curved centerline on the flow is much more important than the effect of the changing cross-sectional shape.

To further confirm this, a straight centerline configuration, shown in Fig. 1(b), was analyzed. This duct has the same distribution of cross-sectional shape as the baseline configuration. As shown by the computed total pressure contours in Fig. 6, the transitioning cross section by itself does not cause any significant distortion of the flow.

It is noted that a small separation bubble was predicted along the right side of the duct between the first and second bends for both the circular cross section and baseline configurations. This is caused by the local adverse streamwise pressure gradient in this region. The marching analysis proceeds through this region using the "FLARE" approximation (Ref. 11). In the PNS analysis, this approximation is implemented by resetting the streamwise velocity to a small positive value if it falls below that value during a marching step. This stabilizes the analysis and allows it to march through small regions of separated flow. The flow details within the recirculation region are not modeled accurately, but if the separation bubble is small its effect on the rest of the flow is usually well modeled.

Vortex Generators in a Diffusing S-Duct (Ref. 2)

Summary of Analysis Method. In efforts to save weight and thereby fuel, it is common to design modern intake ducts to be as short as possible. The designer must therefore be concerned with the possibility of flow separation due to a strong adverse pressure gradient. To alleviate this problem, vortex generators are often used as a flow control device. Most vortex generators in use today are simply small wing sections mounted on the inside of a duct or on the wing of an airplane. Figure 7 shows a typical vortex generator. The vortex generators are inclined at an angle to the oncoming flow to generate the shed vortex. Also, the vortex generator is sized so that the tip lies just outside the edge of the boundary layer. This allows for the best interaction between the shed vortex and the boundary layer. The vortex generators are usually placed in groups of two or more upstream of the problem flow area. The vortex generator will cause a mixing of the high momentum core flow with the low momentum flow in the boundary layer, resulting in a net increase of momentum near the surface. This can delay or even eliminate the separation region.

In order to provide an analytical capability for these flows, the PNS analysis discussed in the previous section has been modified to included a model for vortex generators within a duct flow field (Ref. 12). The transverse momentum equations in the analysis are solved using a stream function - vorticity formulation. The vortex generator model takes advantage of this. The shed vortex is modeled by introducing a source term into the vorticity transport equation that is a function of the vortex generator characteristics. The effect of the drag of the vortex generator is also included in the model. The drag on the wing section is a combination of profile drag, which is due to viscous and pressure effects, and induced drag, which is due to the shed vortex. In this model the profile drag of the vortex generator is neglected in comparison to the induced drag because in the cases studied here the generators were small. The induced drag is then proportional to the vortex strength and the crossflow velocity at a point. This term is included in the governing equations as a negative source term in the primary momentum equation.

Duct Configuration and Inlet Conditions. Figure 8 shows a circular cross sectioned 30° - 30° S-bend diffuser that was tested experimentally both with and without vortex generators (Refs. 13 and 14). For the cases with vortex generators, three pairs were placed well upstream of the separation point. The axial location is indicated in Fig. 8. They were set at incidence angles of ±16° to form three pairs of counter rotating vortices. They were placed along the inside of the bend at azimuthal locations of -38.0°, 0.0°, and +38.0°, as measured from the inside of the bend. The flow in this duct was turbulent with a Mach number of 0.6 and a Reynolds number based on the duct diameter of 1 760 400. The initial conditions were measured at 1.65 duct diameters upstream of the first bend to remove the influence of the bend on the static pressure. The initial boundary layer thickness was 0.1 times the initial duct radius and the area ratio was 1.51.

Computational and Experimental Results. Figure 9(a) shows the computed total pressure coefficient contours at six stations in the duct for the case without vortex generators. The inlet values were used as the reference conditions in computing the total pressure coefficient.

Figure 9(b) shows the experimental results. The maximum and minimum values at each streamwise station are shown on the figure. Comparing the computed and experimental results indicates that the analysis is able to adequately predict the total pressure distortions for the duct. A separated flow region exists in both the experimental and computed results along the lower surface near the inflection point between the two bends. Although the computed results in the separated region will not be correct because of the "FLARE" approximation, the global effect of the separated region

is well modeled. The comparison also shows that at $\theta = 30°$, the fourth contour plot, the experimental results indicate a larger separated region. In the experiment the streamwise separated region was found to be between $\theta = 22°$ and $\theta = 44°$, while in the computation the separated region was between $\theta = 30°$ and $\theta = 54°$. Figures 10 and 11 show comparisons between the computed and experimental secondary velocity profiles at the inflection plane and at the bend exit. The agreement between the two results is very good. At the inflection point the vortex due to the curvature of the centerline is evident in both plots. Also at the inside of the first bend the separated region can be seen in the experimental results, by the region with no data. In the computed results the onset of separation is also evident where there is minimal secondary flow. At the bend exit both results in Fig. 11 show that the separated region is gone by the large amount of flow being swept toward the outside of the second bend. These results differ from those of a nondiffusing circular cross section S-bend, where the vortex due to the centerline curvature is strengthened in the second bend.

Figures 12(a) and (b) show the computed and experimental total pressure coefficients in the S-bend for the case with vortex generators. Again the maximum and minimum values are shown at each streamwise station. At the $\theta = 15°$ point the effect of the vortex generators is evident in the contours. The computed results compare qualitatively well with the experimental results. In both sets of contours the distortion caused by the generators is pushed toward the outside of the first bend, opposed to the pressure driven secondary flow. The total pressure values in these contours are higher than in those of Figs. 9(a) and (b) near the inside wall. This indicates that the vortex generators successfully mixed the high energy flow with the low energy flow to suppress the separation. Although the contours in Figs. 12(a) and (b) still show a very distorted flow, the difference between the maximum and the minimum values is much less here than in the duct without vortex generators. Figures 13 and 14 show the secondary flow development at the inflection plane and at the duct exit. In the experimental results at the inflection plane, the vortices due to the pressure driven secondary flow have washed out the vortices from the vortex generators except near the inside of the first bend. The contour plot indicates that in this region there may still be some interaction between the vortex generator vortices and the ones induced by the pressure difference. The computed results at the inflection point show that all of the vortices have been washed out by the pressure driven secondary flow. This is why the distorted region in the experimental results moves more toward the outside of the bend than in the computed results. At the exit of the bend both the experimental and computed results indicate less secondary flow toward the outside of the second bend than without the vortex generators. Also near the walls they indicate more flow back toward the inside of the second bend. The experimental results show a higher level of flow toward the outside of the bend in the core flow than do the computed results.

High Speed Inlet (Refs. 3 and 4)

Analysis Method. A three-dimensional supersonic viscous marching analysis was used in this study. The code solves the PNS equations for supersonic flow by a linearized block implicit scheme (Ref. 15). The code has been extensively verified at Lewis, with particular emphasis on the calculation of the glancing shock/boundary layer interaction (Ref. 16). The work has demonstrated the numerical capability to realistically model the complex three-dimensional phenomena occurring in this interaction. The work in Ref. 16 also established the importance of grid resolution in modeling this interaction.

Intake Configuration. A schematic drawing of the mixed compression intake is shown in Fig. 15. This inlet was originally designed using the method of characteristics with the surfaces corrected for boundary layer displacement effects. It is rectangular in cross section and has a pre-compression ramp and three compression ramps external to the cowl. Operation at angle of attack generates a shock wave at the leading edge of the pre-compression plate. The pre-compression and ramp shocks were designed to fall outside the cowl lip at the design Mach number of 5.0. The shock generated at the cowl lip is cancelled at the ramp shoulder and the cowl is contoured to provide further internal compression. A swept sideplate runs from the leading edge of the pre-compression plate to the leading edge of the cowl to minimize the drag generated by compressed flow spilling over the sides.

Two-Dimensional Computed Results. The PNS code was initially run two-dimensionally at a free stream Mach number of 5.0, angle of attack of 9.0°, and a Reynolds number of 2.5×10^6. Fig. 16 shows the computed Mach number profiles at various positions. Proper cancellation of the cowl shock at the shoulder is observed in spite of the extremely large displacement correction. The figure also shows the extremely thick boundary layer that forms on the ramp surface; i.e., about 1/3 of the flow into the inlet is boundary layer. Near the inlet throat, the two boundary layers are merged. Predictions of static pressure rise and total pressure loss through the compression system agree well with method of characteristic results corrected for boundary layer effects.

Three-Dimensional Computed Results. The Mach 5.0 inlet described in a previous section was analyzed three-dimensionally using the PNS analysis program. The free stream conditions for the three-dimensional case were the same as those in the two-dimensional inlet case. The computations were performed on an 80 by 60 cross-sectional grid, which corresponds to the levels of grid resolution required for accurate modeling of glancing shock boundary layer interactions (Ref. 16). The inviscid Mach

number aft of the pre-compression shock is on the order of 4.0, which is very close to our established data base.

The results from the three-dimensional calculation are presented in Figs. 17 to 20. At the top of each figure is a schematic of the inlet, with the location of the cross-sectional plane given by a vertical line and a prescribed distance from the inlet leading edge. The bottom of the figure shows the flowfield in a cross section of the inlet; the ramp surface is at the bottom, the cowl surface at the top, and sideplates are on both sides. Because of flow symmetry, only half of the inlet was calculated. The left side of the figure shows Mach number contours, while the right side shows secondary velocity within the cross-sectional plane. The figures proceed from a location just downstream from the inlet leading edge to a location inside the cowl near the throat. On the solid surface of the ramp, cowl and sideplate, one will note the development and growth of the boundary layer by a concentration of Mach contours near these surfaces. Shock waves are noted by a concentration of Mach contours away from the solid surfaces. They can also be detected by an abrupt change in the secondary velocity vectors. In this calculation, the compression shocks and the Mach contours are parallel to the ramp and cowl surfaces.

Entering the region of the compression ramps, Fig. 17 shows the flowfield just downstream of the first ramp. The shock generated by this ramp is evident in the Mach contours; near the center of the flowfield this shock is flat while near the sideplate the shock forms a characteristic λ as it interacts with the boundary layer of the sideplate. In the secondary velocity vectors, one sees a cross flow being induced along the sideplate and feeding forward of the inviscid shock location. Near the cowl lip, the flow field appears as Fig. 18. The secondary velocity vectors also show extremely strong flow along the sideplate, while the Mach number contours show the sideplate boundary layer to be highly distorted. The boundary layer has been thickened in the vicinity of the shock waves and thinned in the corner formed by the ramp and sideplate. The secondary velocity vectors show flow being drawn along the ramp surface into this corner. The boundary layer along the ramp surface is quite thick and corresponds to the thickness predicted in the two-dimensional calculations. The strong secondary flows induced by the multiple shock interactions persist even though the shock waves have left the flow domain over the cowl. The flowfield from the inlet leading edge to the cowl lip has been shaped by the thick boundary layer that grows on the ramp and sideplate and the multiple shock interactions that occur on the sideplate due to the compression ramps. The flow is highly three-dimensional at the cowl lip with low energy boundary layer flow being swept up along the sideplate. As the flow enters the cowl, Fig. 19 shows that a shock wave is generated by the cowl lip. This shock, indicated by the horizontal lines in the Mach contours, moves down through the flow field as shown in Fig. 20. The strong secondary flow moving up the sideplate encounters the internal cowl surface and the secondary velocity vectors indicate that this flow turns through the corner formed by the cowl and sideplate. Figure 20 shows that two things happen as the secondary flow turns this corner; first, the secondary flow rolls up into a vortex, and second, the low energy flow is concentrated in the corner. The internal surface of the cowl has been shaped to further compress the flow. As the low energy flow in the corner is subjected to the adverse pressure gradient created by this turning, a large separation occurs. The last calculated cross section is shown in Fig. 20. The shock from the cowl is about to hit the ramp surface, while the large separation region exists in the corner. The secondary flow has rolled into a vortex near the sideplate, while along the ramp, flow continues into the corner.

Even though the FLARE approximation was employed, the magnitude of the separation was so severe that the analysis did not march further. The existence of a large separation in the corner of the inlet would probably trigger an inlet unstart at these conditions. Even if the inlet remained started, the existence of the vortex near the sideplate and the distortion of the sideplate boundary layer as shown in Fig. 20 would pose major problems for the propulsion system.

Experimental Observations. A subscale model of the Mach 5 inlet was tested at Lewis. Figure 21 shows oil flow results which indicate that the flow near the ramp surface is drawn in towards the sideplates. This figure shows velocity vectors on the surface of the ramp from the third ramp to the cowl. In the lower left corner of the figure the computed velocity vectors near the ramp surface are shown. The velocity vectors also indicate that flow is drawn in toward the sideplate because of the glancing sidewall boundary layer interactions. This is the first qualitative verification of the results of the Mach 5.0 inlet study.

Additional confirmation of the strong secondary flow patterns computed for the inlet may be found in Ref. 17. In Ref. 17, a two-dimensional mixed compression Mach 3.05 intake was experimentally tested. Total pressure measurements were obtained at a number of stations within the inlet. Figure 22 shows total pressure contours downstream of the normal shock which clearly indicate vortex-like flow. These measured flow contours yield further qualitative confirmation of the PNS computed results described above.

Sideplate Spillage Computations Further development of the PNS solver (Ref. 4) has yielded the capability of analyzing the flow spilled over the intake side plates. Initial results obtained are shown in Figs. 23 and 24. The static pressure distribution both upsteam and downstream of the cowl are shown.

CONCLUSIONS

Computer results of the flow distortion and total pressure variation in complex intakes were reviewed. The analyses were performed using parabolized Navier-Stokes marching analyses. The first set of results were for intakes with centerline curvature and cross-sectional transitioning. It was concluded that the distortions and losses in the S-shaped duct were primarily related to the centerline curvature, whereas the transitioning cross section had little effect on flow quality and pressure loss. The second set of results reviewed were for a diffusing S-duct with subsonic entrance flow. Numerical analysis of the flow was performed both with and without vortex generators located near the entrance of the diffuser. The generators were found to be computationally effective in suppressing the flow separation that occurred previously. Although flow distortion was not eliminated, the difference between the maximum and minimum total pressure at the compressor face was significantly reduced. The computed results compared favorably with the experimental data. Further analytical refinements are needed to improve the vortex generator model in the analysis.

The final set of results presented were for a Mach 5.0 intake. Both a two-dimensional and a three-dimensional version of a supersonic PNS code were run. The two-dimensional version verified the original method of characteristics design, while the three-dimensional version revealed entirely new information relative to the nature of the flow. High amounts of distortion, strong secondary flows and flow separation were computed in the supersonic intake. These phenomena are caused by thick boundary layers which develop on the inlet surfaces and their interaction with the shock waves of the compression system. The results from these calculations indicate that the sideplates require redesigning. In addition, provisions for bleeding the sideplate and the corner may be required to improve flow quality. In that case, a compromise would be necessary between recovery, distortion, spillage drag and bleed drag. Limited experimental data provided some verification of the occurrence of secondary flows in the intake.

REFERENCES

1. Towne, C.E., and Schum, E.F., "Application of Computational Fluid Dynamics to Complex Inlet Ducts," AIAA Paper 85-1213, July 1985.

2. Kunik, W.G., "Application of a Computational Model for Vortex Generators in Subsonic Internal Flows," AIAA Paper 86-1458, June 1986.

3. Benson, T J., "Three-Dimensional Viscous Calculation of Flow in a Mach 5.0 Hypersonic Inlet," AIAA Paper 86-1461, June 1986.

4. Kim, Y.N., Buggeln, R.C., and McDonald, H., "Numerical Analysis of Some Supersonic Viscous Flows Related to Inlet and Nozzle Systems," AIAA Paper 86-1597, June 1986.

5. Briley, W.R., and McDonald, H., "Analysis and Computation of Viscous Subsonic Primary and Secondary Flows," AIAA Paper 79-1453, July 1979.

6. Levy, R., McDonald, H., Briley, W.R., and Kreskovsky, J.P., "A Three-Dimensional Turbulent Compressible Subsonic Duct Flow Analysis for Use with Constructed Coordinate Systems," AIAA Paper 80-1398, July 1980.

7. Levy, R., Briley, W.R., and McDonald, H., "Viscous Primary/Secondary Flow Analysis for Use with Nonorthogonal Coordinate Systems," AIAA Paper 83-0556, Jan. 1983.

8. Towne, C.E., "Computation of Viscous Flow in Curved Ducts and Comparison With Experimental Data," AIAA Paper 84-0531, Jan. 1984.

9. Anderson, B.H., "Three-Dimensional Viscous Design Methodology for Advanced Technology Aircraft Supersonic Inlet Systems," AIAA Paper 84-0194, Jan. 1984.

10. Vakili, A., Wu, J.M., Hingst, W.R., and Towne, C.E., "Comparison of Experimental and Computational Compressible Flow in an S-Duct," AIAA Paper 84-0033, Jan. 1984.

11. Reyhner, T.A., and Flugge-Lotz, I., "The Interaction of a Shock Wave with a Lamina Boundary Layer," Int. J. Non-Linear Mechanics, vol. 3, no. 2, June 1968, pp. 173-199.

12. Levy, R., "Vortex Generator Modeling," NASA CR- Report in Preparation, 1986.

13. Vakili, A.D., Wu, J.M., Liver, P., and Bhat, M.K., "Experimental Investigation of Secondary Flow in a Diffusing S-Duct," NASA CR- Report in Preparation, 1986.

14. Vakili, A.D., Wu, J.M., Liver, P., and Bhat, M.K., "Flow Control in a Diffusing S-Duct," AIAA Paper 85-0524, Mar. 1985.

15. Buggeln, R.C., McDonald, H., Levy, R., and Kreskovsky, J.P., "Development of a Three-Dimensional Supersonic Inlet Flow Analysis," NASA CR-3218, 1980.

16. Anderson, B.H., and Benson, T.J., "Numerical Solution to the Glancing Sidewall Oblique Shock Wave/Turbulent Boundary Layer Interaction in Three Dimensions," AIAA Paper 83-0136, Jan. 1983.

17. Fisher, S.A., "Three-Dimensional Flow Effects in a Two-Dimensional Air Intake with Mixed Supersonic Compression," Seventh International Symposium on Air-Breathing Engines, AIAA, 1985, pp. 118-124.

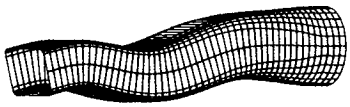

(a) Baseline.

(b) Straight centerline.

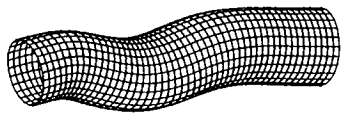

(c) Circular cross-section

Figure 1. - Inlet configurations.

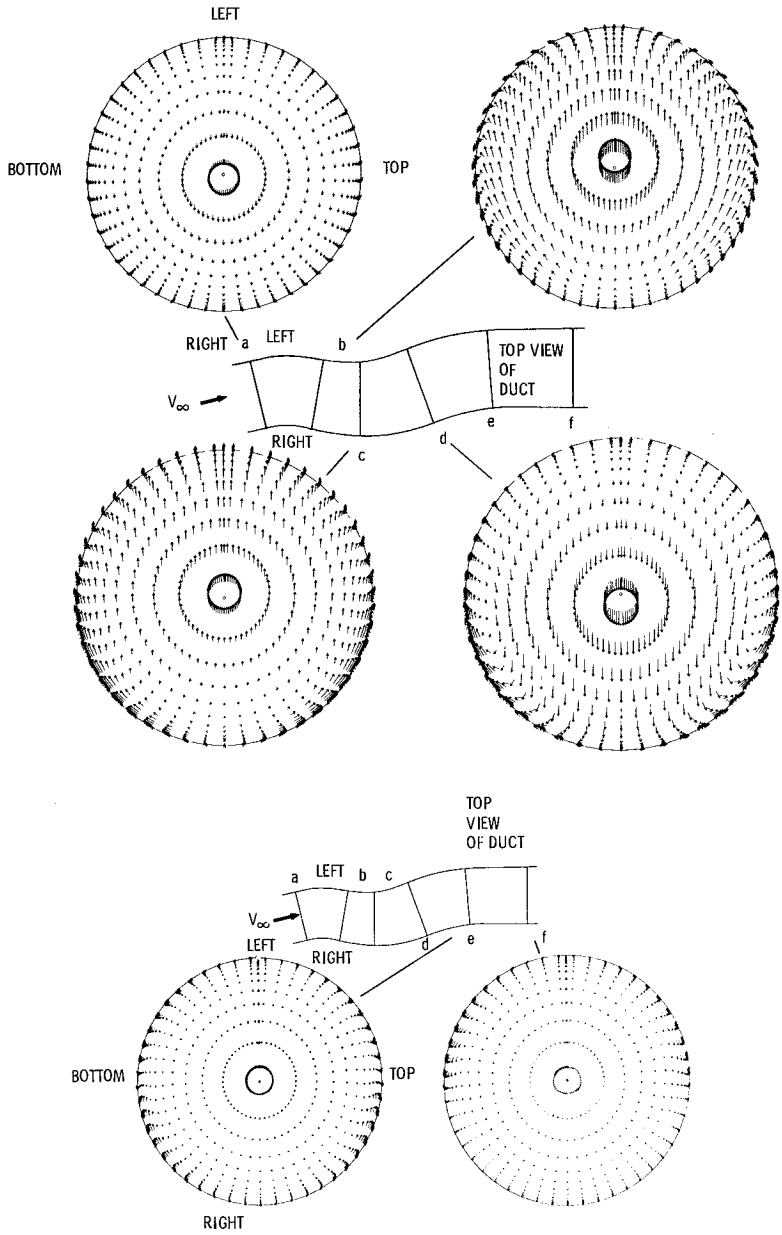

Figure 2. - Computed cross stream velocities in circular cross-section configuration, $M = 0.5$, $\delta = 0.056$, 50x50x105 mesh.

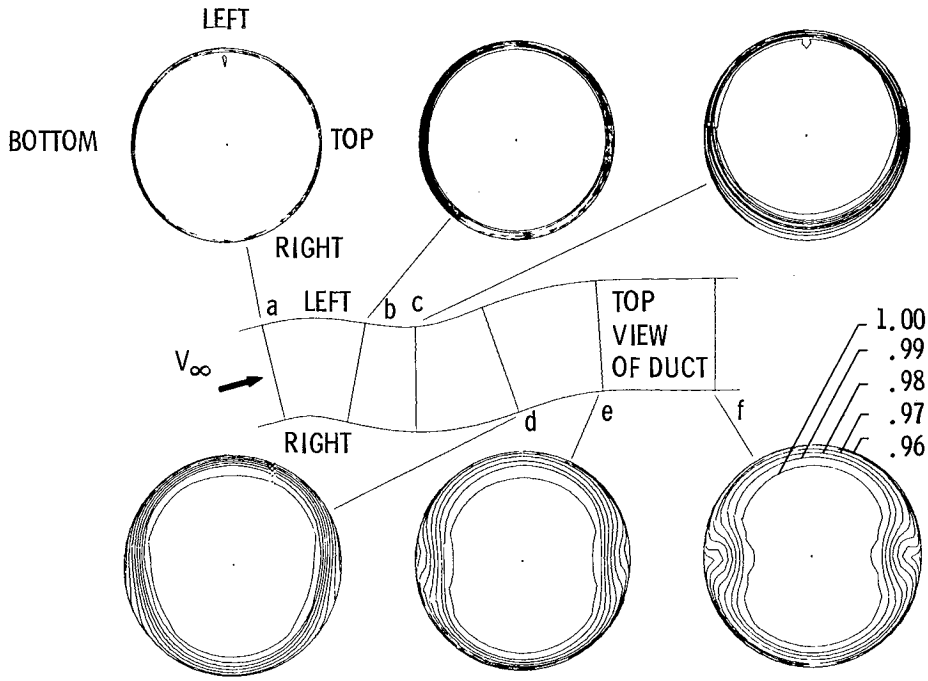

Figure 3. - Computed total pressure contours in circular cross-section configuration, $M = 0.5$, $\delta = 0.056$, 50x50x105 mesh.

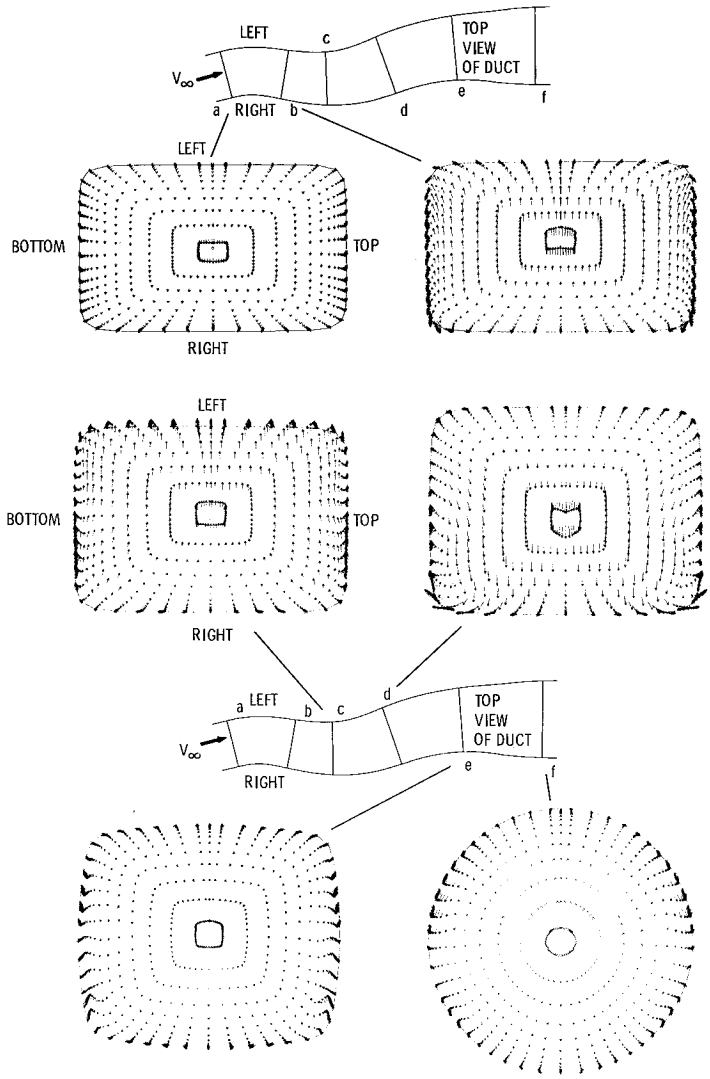

Figure 4. - Computed cross stream velocities in baseline configuration, M = 0.5, δ = 0.048, 50x50x105 mesh.

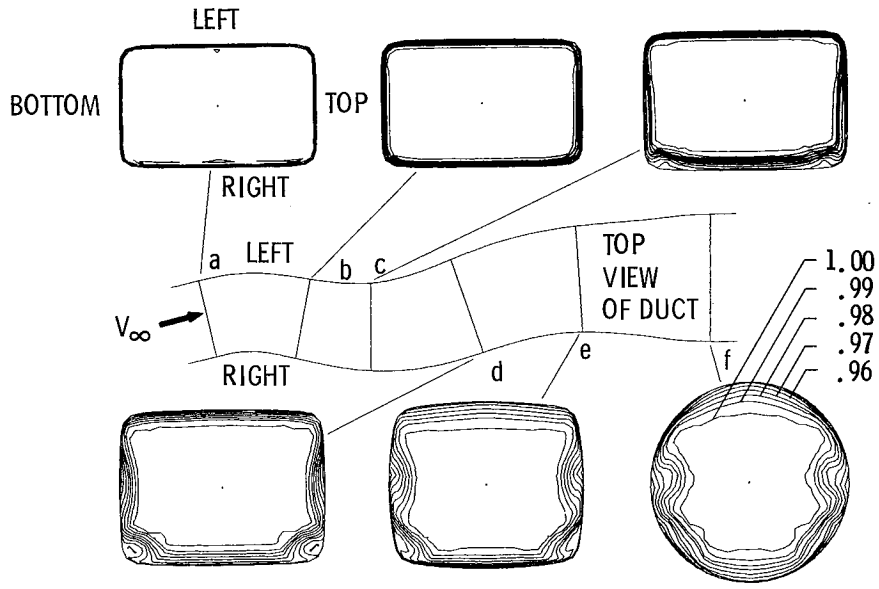

Figure 5. - Computed total pressure contours in baseline configuration, M = 0.5, δ = 0.048, 50x50x105 mesh.

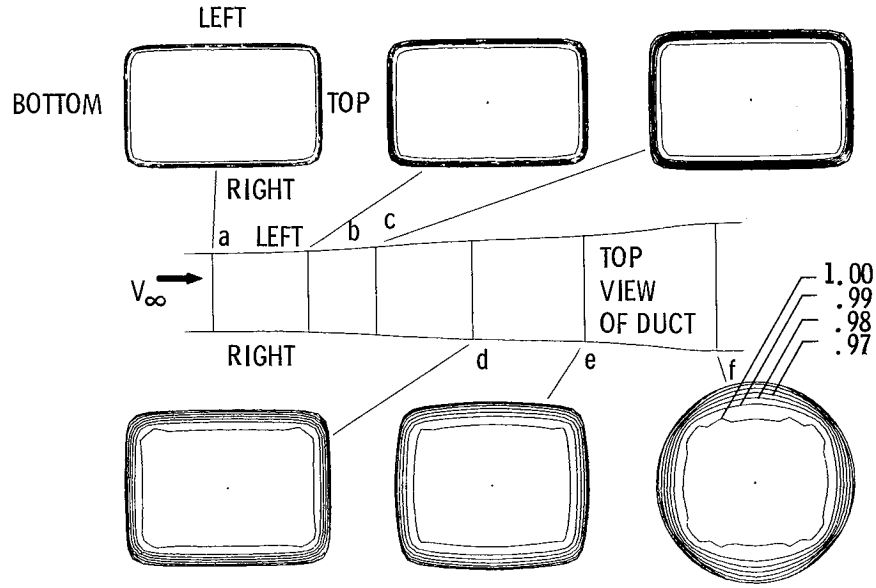

Figure 6. - Computed total pressure contours in straight centerline configuration, M = 0.5, δ = 0.048, 50x50x105 mesh.

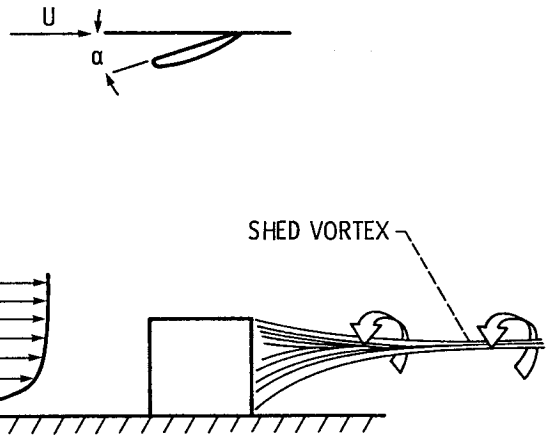

Figure 7. - A typical vortex generator.

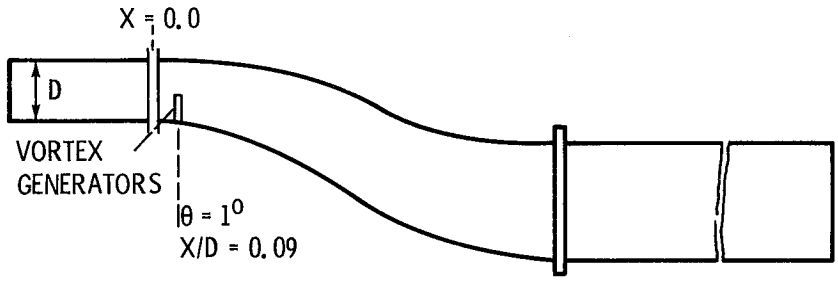

Figure 8. - Schematic of diffusing S-duct showing the axial location of the vortex generators.

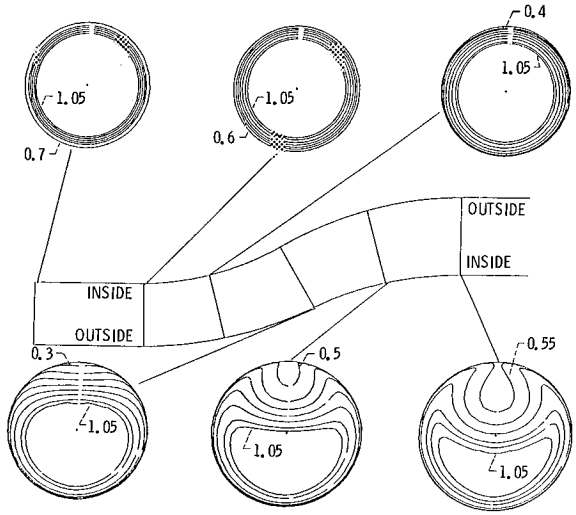

(a) Computed results.

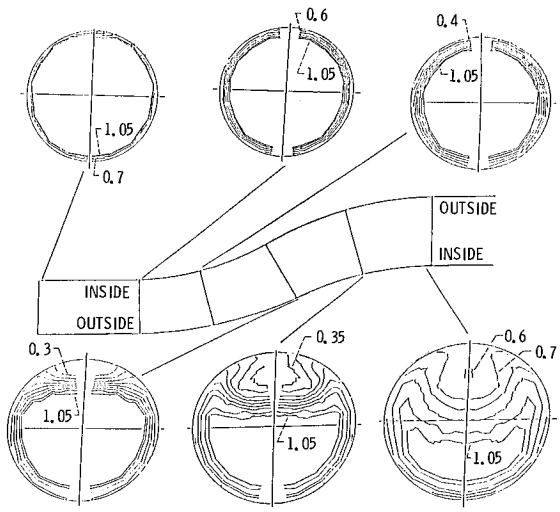

(b) Experimental results.

Figure 9. – Total pressure coefficient contours for S-duct without v. g. 's.

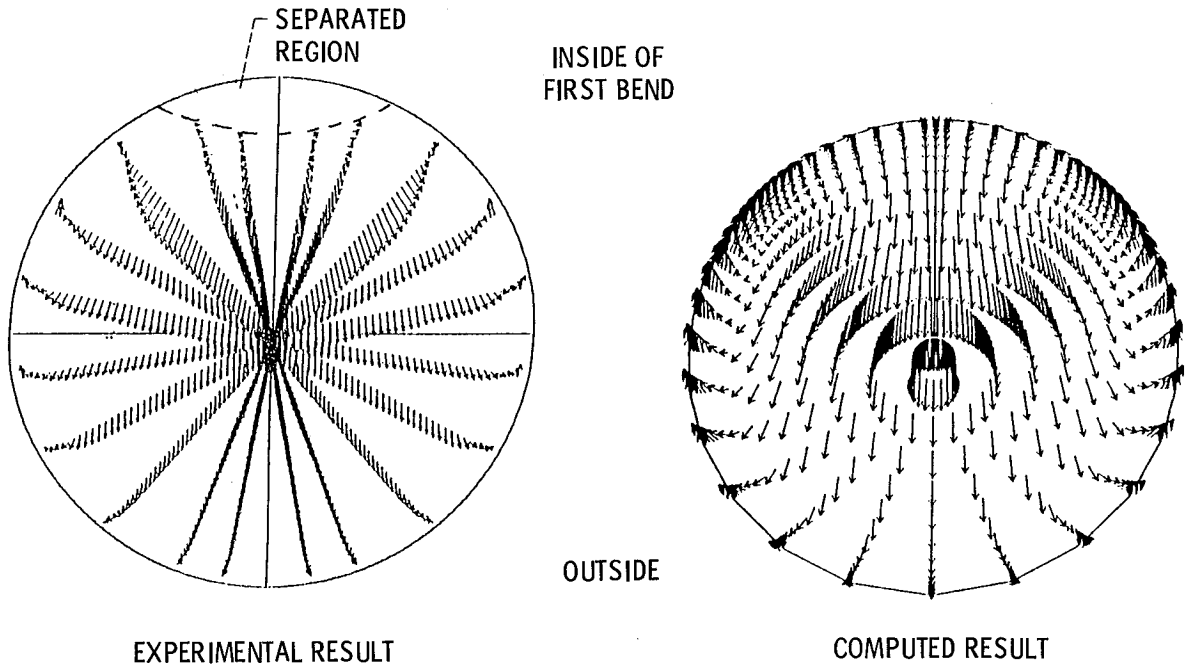

Figure 10. - Comparison of secondary flow at the inflection plane for S-duct without v.g.'s.

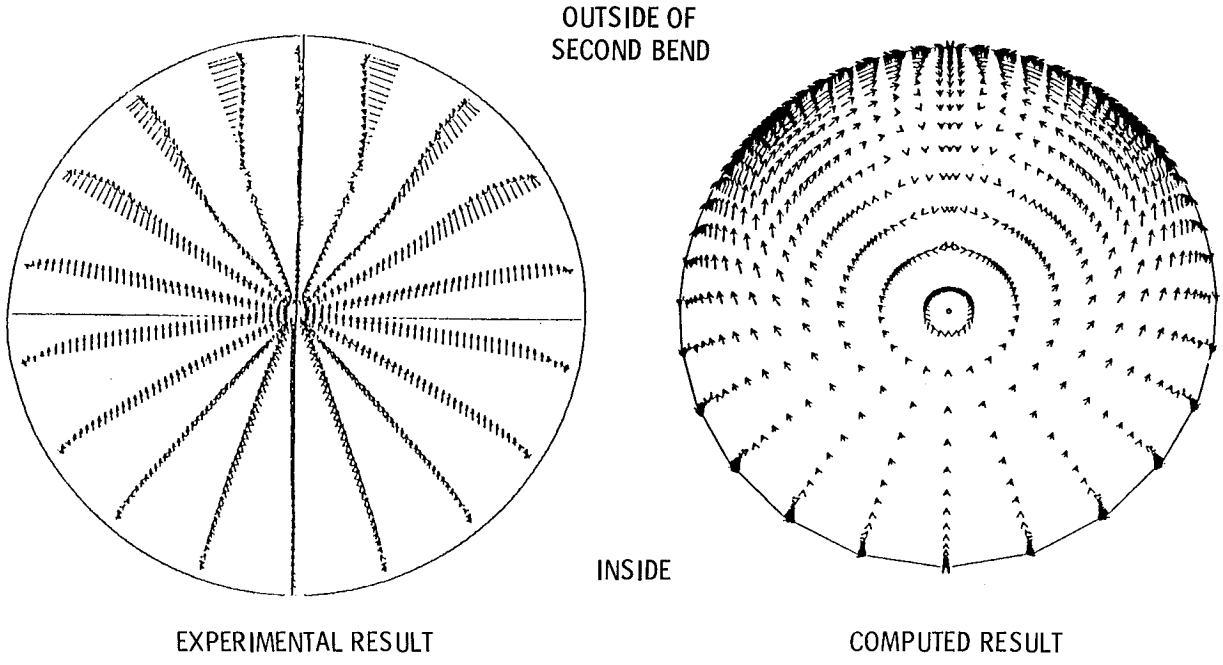

Figure 11. - Comparison of secondary flow at the exit plane for S-duct without v.g.'s.

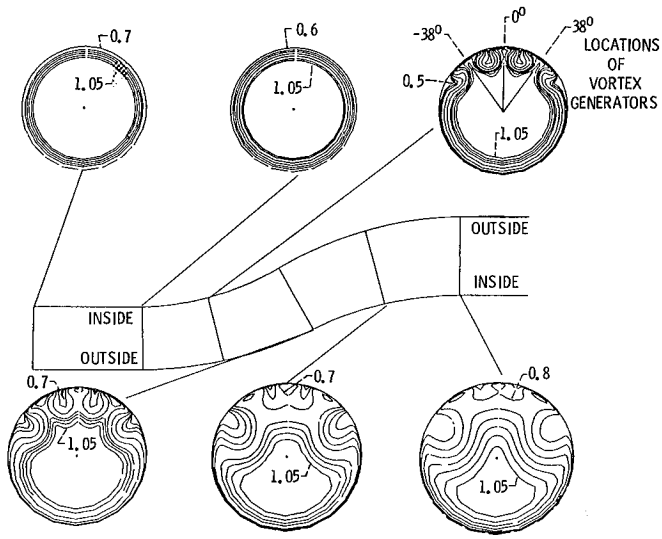

(a) Computed results.

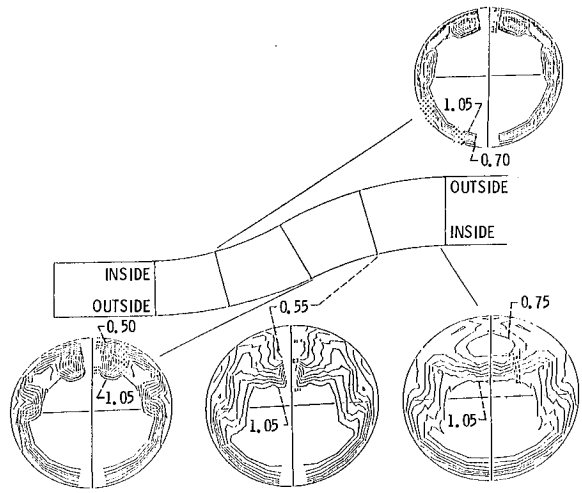

(b) Experimental results.

Figure 12. - Total pressure coefficient contours for S-duct with v.g.'s.

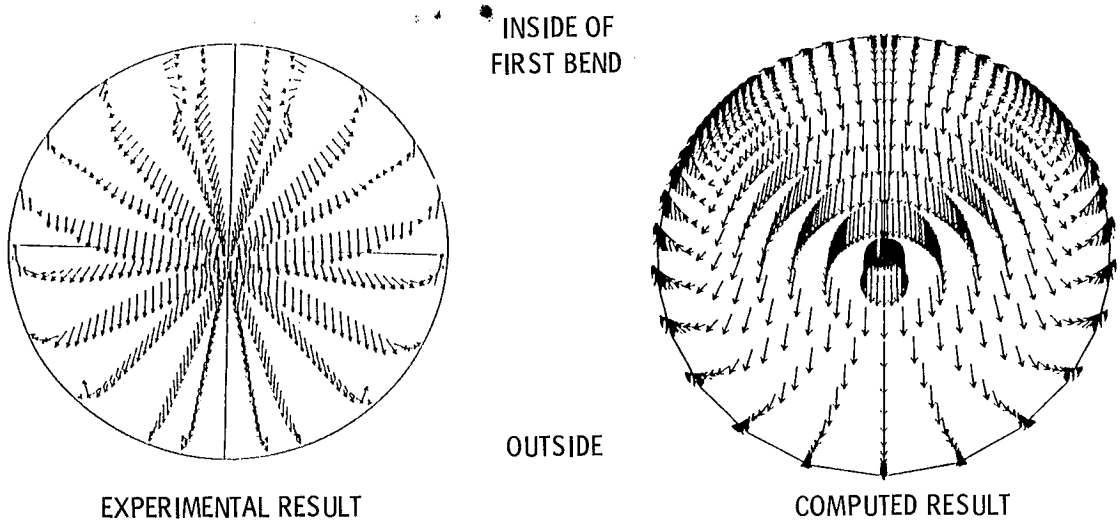

Figure 13. - Comparison of secondary flow at the inflection plane for S-duct with v. g.'s.

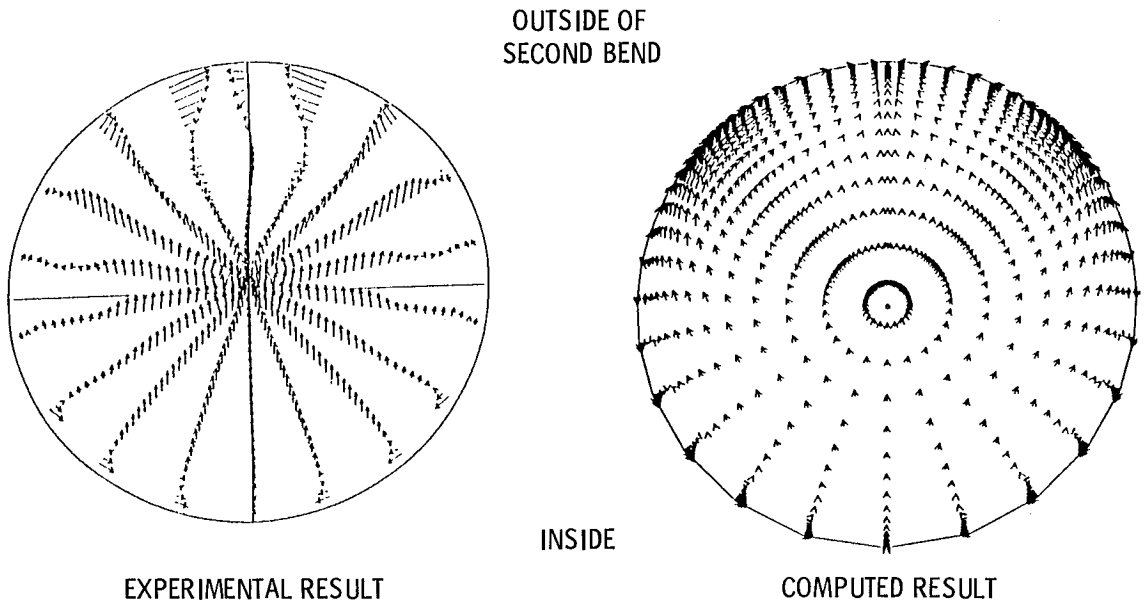

Figure 14. - Comparison of secondary flow at the exit plane for S-duct with v. g.'s.

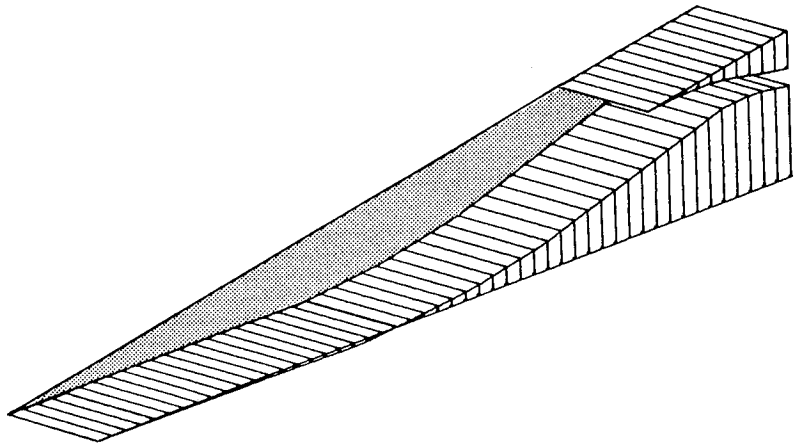

Figure 15. - Mach 5.0 Hypersonic Inlet Geometry.

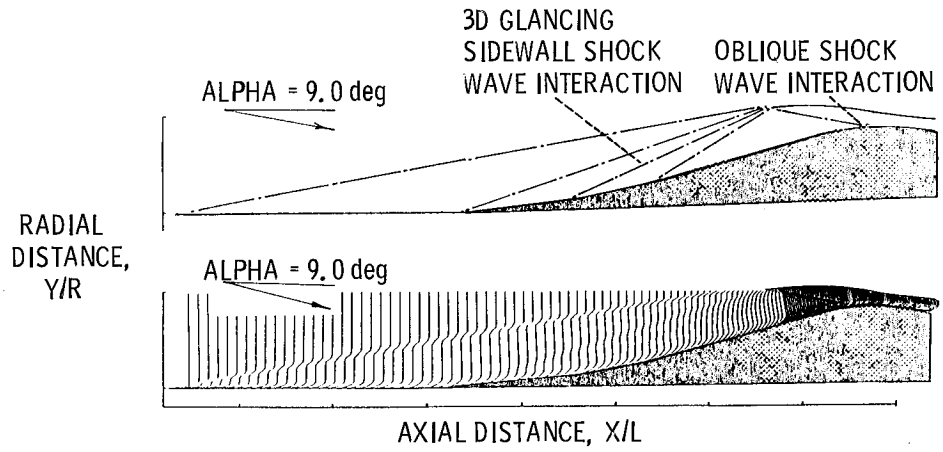

Figure 16. - Shock structure and 2D Mach number profiles.

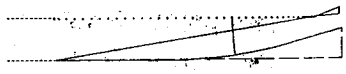

STATION 229
X/HC = 0.4347E 01

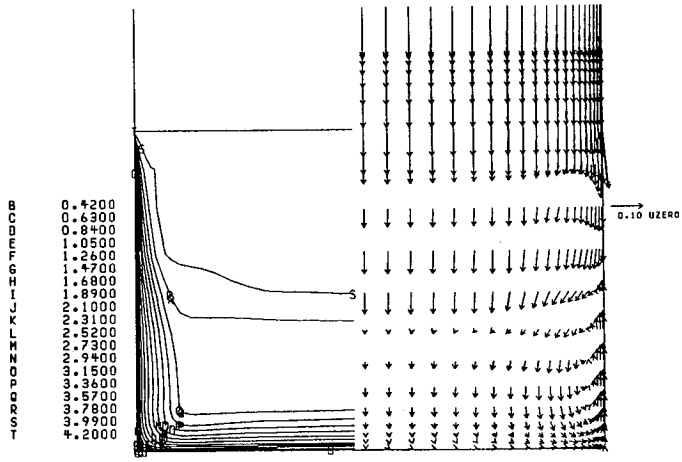

Figure 17. - Mach number contours and secondary velocity vectors aft of first ramp.

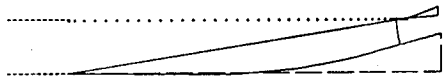

STATION 369
X/HC = 0.6158E 01

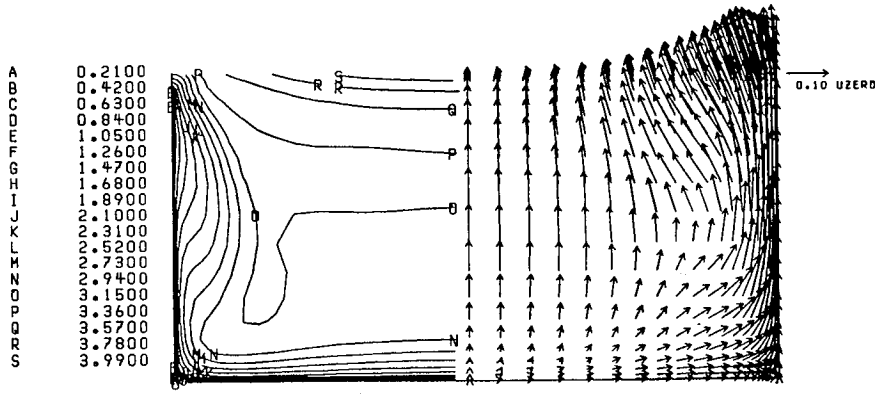

Figure 18. - Mach number contours and secondary velocity vectors before cowl lip.

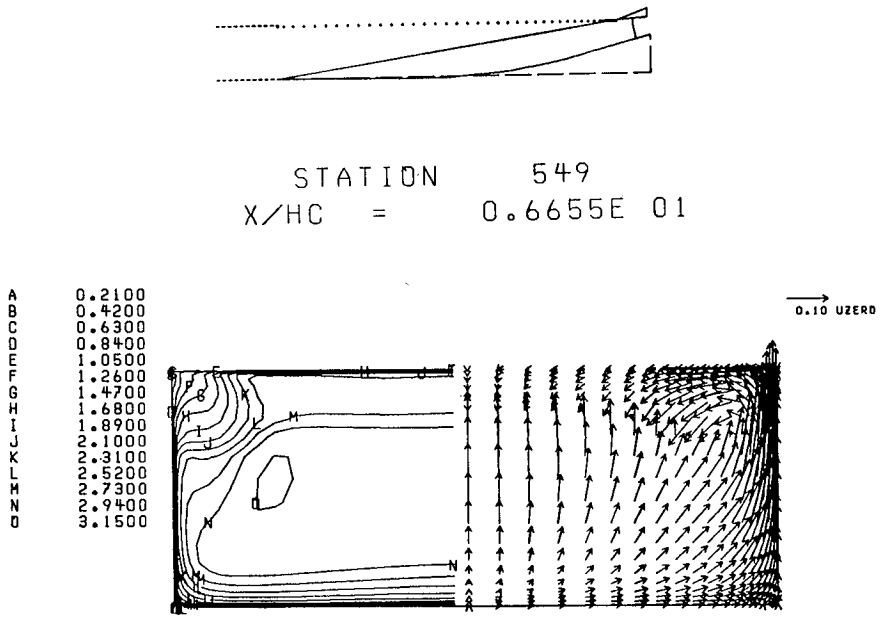

Figure 19. - Mach number contours and secondary velocity vectors aft of cowl lip.

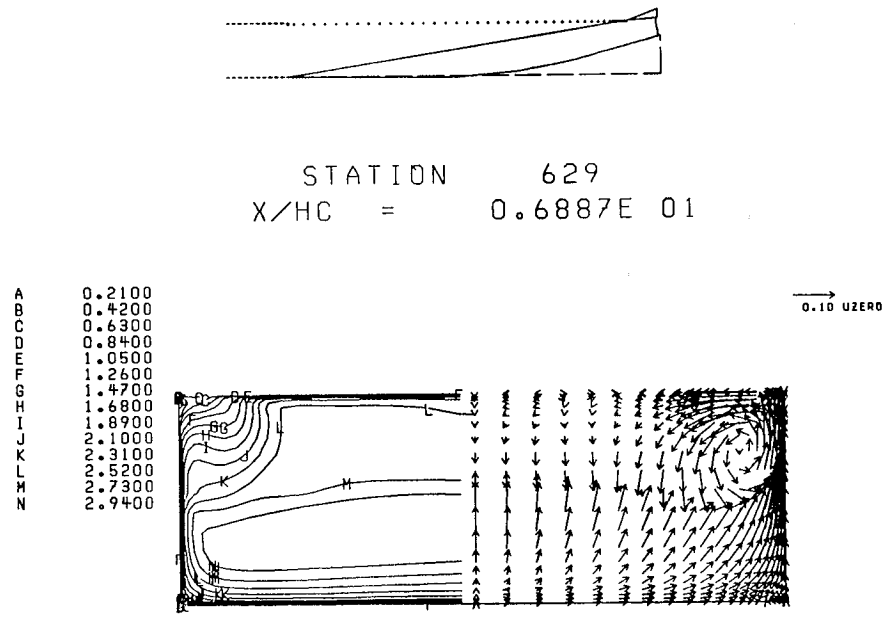

Figure 20. - Mach number contours and secondary velocity vectors at corner separation.

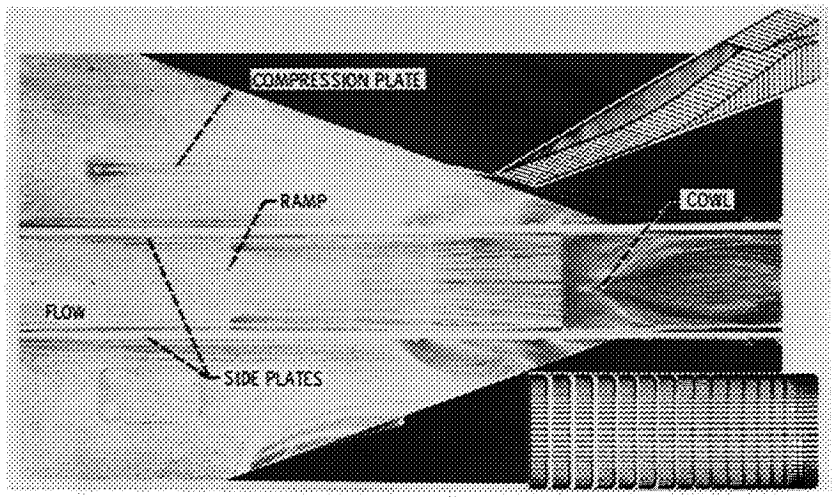

Figure 21. - Surface oil flow and calculated velocity vectors for inlet ramp surface.

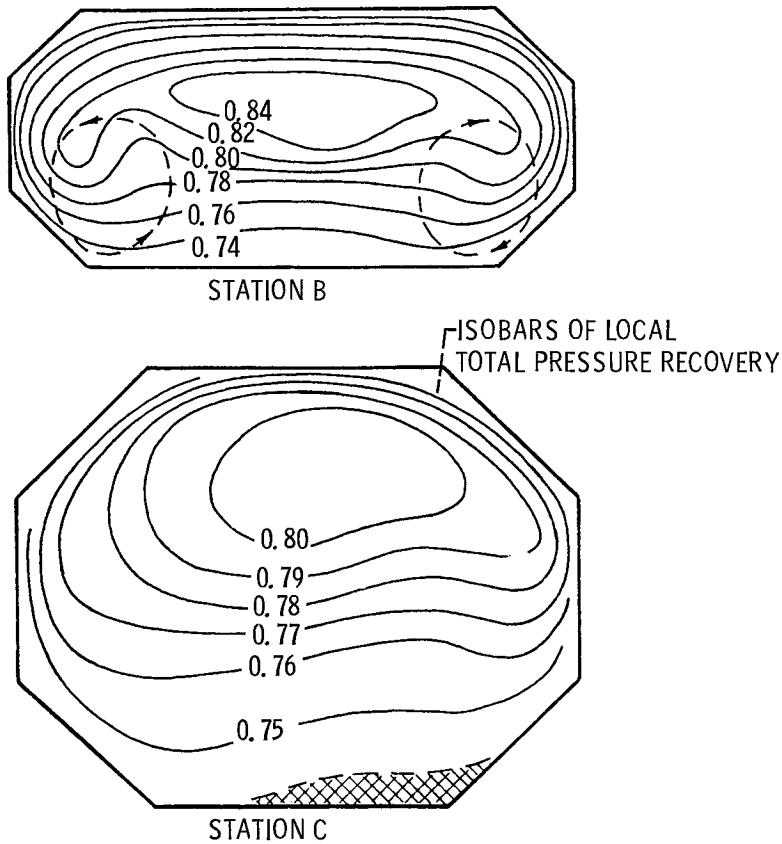

Figure 22. - Flow Distributions in Subsonic Diffuser.

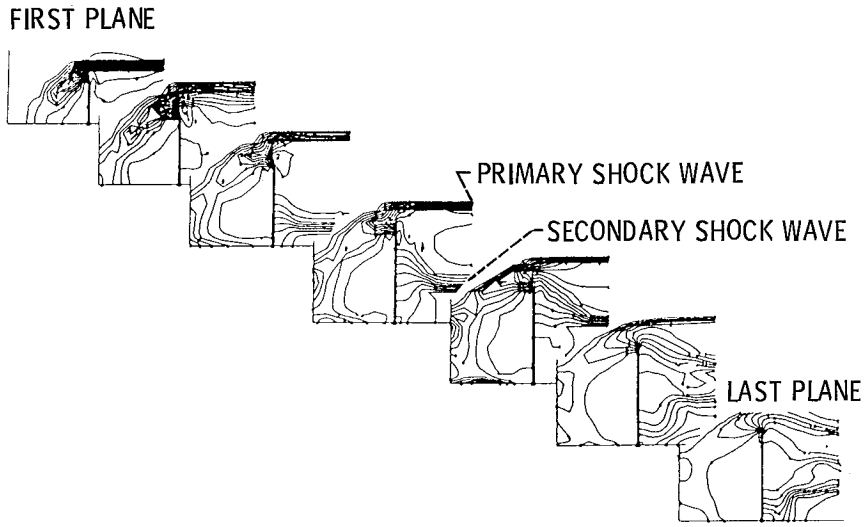

Figure 23. - Static pressure distribution upstream of the cowl entrance in planes normal to the 'Streamwise' direction. Planes from left to right proceed downstream.

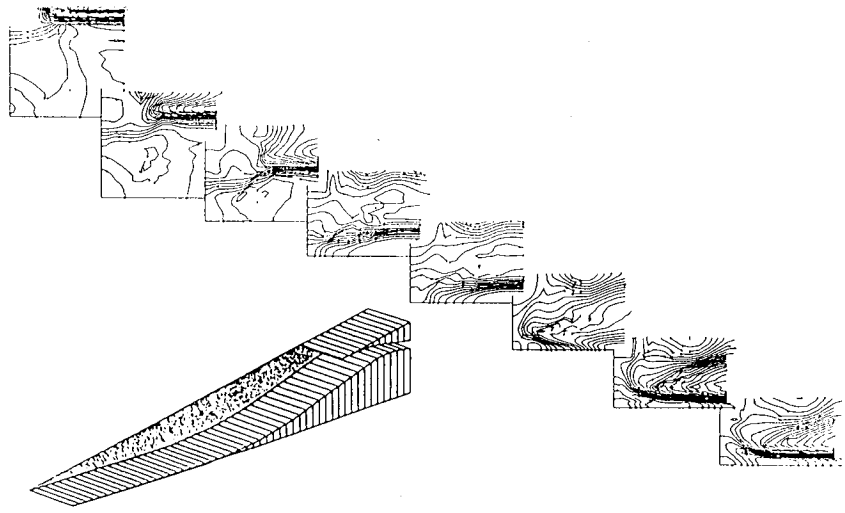

Figure 24. - Static pressure distribution downstream of the cowl entrance.

1. Report No.	2. Government Accession No.	3. Recipient's Catalog No.
NASA TM-88831		

4. Title and Subtitle	5. Report Date
Viscous Analyses for Flow Through Subsonic and Supersonic Intakes	6. Performing Organization Code 505-62-21

7. Author(s)	8. Performing Organization Report No.
Louis A. Povinelli and Charles E. Towne	E-3209
	10. Work Unit No.

9. Performing Organization Name and Address	11. Contract or Grant No.
National Aeronautics and Space Administration Lewis Research Center Cleveland, Ohio 44135	13. Type of Report and Period Covered Technical Memorandum
12. Sponsoring Agency Name and Address	14. Sponsoring Agency Code
National Aeronautics and Space Administration Washington, D.C. 20546	

15. Supplementary Notes

Prepared for the AGARD Propulsion and Energetics Panel Meeting on Engine Response to Distorted Inflow Conditions, Munich, Germany, September 8-9, 1986. Guest Paper.

16. Abstract

A parabolized Navier-Stokes code was used to analyze a number of diffusers typical of a modern inlet design. The effect of curvature of the diffuser centerline and transitioning cross sections was evaluated to determine the primary cause of the flow distortion in the duct. Results are presented for S-shaped intakes with circular and transitioning cross sections. Special emphasis is placed on verification of the analysis to accurately predict distorted flow fields resulting from pressure-driven secondary flows. The effect of vortex generators on reducing the distortion of intakes is presented. Comparisons of the experimental and analytical total pressure contours at the exit of the intake exhibit good agreement. In the case of supersonic inlets, computations of the inlet flow field reveal that large secondary flow regions may be generated just inside of the intake. These strong flows may lead to separated flow regions and cause pronounced distortions upstream of the compressor.

17. Key Words (Suggested by Author(s))	18. Distribution Statement
Inlet; Intakes; Viscous analysis; Intake distortion	Unclassified - unlimited STAR Category 02

19. Security Classif. (of this report)	20. Security Classif. (of this page)	21. No. of pages	22. Price*
Unclassified	Unclassified		

*For sale by the National Technical Information Service, Springfield, Virginia 22161